

See discussions, stats, and author profiles for this publication at: <https://www.researchgate.net/publication/236014978>

Direct atomic observation in powdered 4H-Ba_{0.8}Sr_{0.2}Mn_{0.4}Fe_{0.6}O_{2.7}

ARTICLE *in* CHEMISTRY OF MATERIALS · FEBRUARY 2013

Impact Factor: 8.35 · DOI: 10.1021/cm303609r

CITATION

1

READS

76

8 AUTHORS, INCLUDING:



Aúrea Varela

Complutense University of Madrid

46 PUBLICATIONS 287 CITATIONS

[SEE PROFILE](#)



Sorin Lazar

McMaster University

71 PUBLICATIONS 1,002 CITATIONS

[SEE PROFILE](#)



Jose M. Gonzalez-Calbet

Complutense University of Madrid

83 PUBLICATIONS 1,101 CITATIONS

[SEE PROFILE](#)



Marina Parras

Complutense University of Madrid

118 PUBLICATIONS 1,060 CITATIONS

[SEE PROFILE](#)

Direct Atomic Observation in Powdered 4H- $\text{Ba}_{0.8}\text{Sr}_{0.2}\text{Mn}_{0.4}\text{Fe}_{0.6}\text{O}_{2.7}$

María Hernando,[†] Laura Miranda,[†] Aurea Varela,[†] Khalid Boulahya,[†] Sorin Lazar,[‡] Derek C. Sinclair,[§] José M. González-Calbet,^{*,†} and Marina Parras^{*,†}

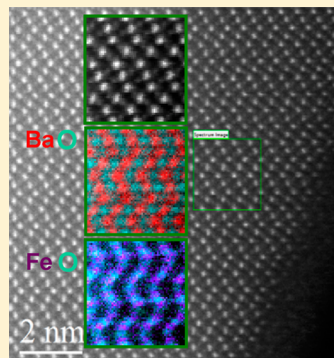
[†]Departamento de Química Inorgánica, Facultad de Químicas, Universidad Complutense, Campus de Excelencia Internacional Moncloa, E-28040-Madrid, Spain

[‡]FEI Company, 5600 KA Eindhoven, The Netherlands

[§]Department of Materials Science & Engineering, University of Sheffield, Mappin Street, Sheffield S1 3JD, United Kingdom

S Supporting Information

ABSTRACT: A new hexagonal polytype in the $\text{BaMn}_{1-x}\text{Fe}_x\text{O}_{3-\delta}$ system has been stabilized. Powdered $\text{Ba}_{0.8}\text{Sr}_{0.2}\text{Mn}^{\text{IV}}_{0.4}\text{Fe}^{\text{III}}_{0.6}\text{O}_{2.70}$ crystallizes in the 4H hexagonal polytype (space group $P6_3/mmc$) according to X-ray diffraction. HAADF images and chemical maps with atomic resolution have been obtained by combining Cs-corrected electron microscopy and EELS spectroscopy. The structure is formed by dimers of face-sharing octahedra linked by corners. EELS data show a random distribution of the transition metals ions identified by Fe and Mn-L2,3 chemical maps. A systematic difference in contrast observed in the O-K signal mapping suggests that anion deficiency is randomly located along the hexagonal layers in agreement with ND data. The magnetic structure consists of ferromagnetic sheets with the magnetic moments aligned along the x -axis and coupled antiferromagnetically along the c -axis.



KEYWORDS: corrected aberration electron microscopy, energy electron loss spectroscopy, hexagonal perovskites

INTRODUCTION

Prompted by the need to control properties of technological promise such as ferroelectricity in hexagonal perovskites, considerable work on the compositional variations of these polytypes has been carried out in order to establish the most adequate relationship between structural type and electric and magnetic properties to get useful devices. The paramount role played by the ratio of hexagonal and cubic layers defining the stacking sequence of a given polytype was early recognized, and efforts devoted to search hexagonal perovskites containing different cubic/hexagonal stacking sequences have led to developing dielectric resonators at microwave frequencies with high permittivity and moderate losses.^{1,2} The wide variety of arrangements of corner/face sharing octahedral building blocks in ABO_3 perovskite-like compounds is an excellent example of the diversity and flexibility of perovskite-based crystal structures. In fact, the stacking sequence of the AO_3 layers in ABO_3 perovskites can be cubic or hexagonal leading to the 3C- and 2H- ABO_3 structural types. These two structures represent the two “extreme” polytypes of the perovskite structure. The first one is based only on cubic close packed (...ccp...) AO_3 layers. The structure consists of a 3D array of corner sharing BO_6 octahedra. This structure is stable if the structural tolerance factor t is close to 1 ($t = d_{\text{A-O}}/\sqrt{2d_{\text{B-O}}}$, where $d_{\text{A-O}}$ and $d_{\text{B-O}}$ represent the average cation–oxygen interatomic distances of the A- and B-sites, respectively).³ When the A cationic size is large enough, t becomes greater than unity leading to perovskites based on hexagonal close

packing of AO_3 layers which give rise to infinite 1D chains of face-sharing octahedra parallel to the c -axis. This structure, adopted by BaMnO_3 , is known as the 2H-type⁴ (two layer hexagonal cell). Between these two extremes, a wide variety of perovskite based structures can be obtained by combination of different cubic (c) and hexagonal (h) stacking layer sequences, leading to several polytypes containing both corner- and face-sharing octahedra. These hexagonal polytypes are denoted by the symbols $n\text{H}$ or $n\text{R}$, where n stands for the number of layers and H or R for the hexagonal or rhombohedral symmetry of the unit cell.

Keeping manganese at the B perovskite site, the tolerance factor can be modified by substitutions at the A sublattice in order to modify the $d(\text{A-O})$ distance. A representative example is 4H- SrMnO_3 ,⁵ an intermediate polytype between 2H- BaMnO_3 and 3C- CaMnO_3 with 50% hexagonal and 50% cubic stacking: ...chch..., a sequence which according to Negas⁶ can be stabilized in the $\text{Ba}_{1-x}\text{Sr}_x\text{MnO}_3$ system for $x = 0.5$ and $x = 0.9$. Oxygen deficiency in the 2H structural type is usually accommodated by the introduction of cubic deficient $\text{BaO}_{3-\delta}$ layers leading to the stabilization of different hexagonal polytypes. The introduction of anionic vacancies modifies the layer stacking sequence since, obviously, the $\text{Mn}^{4+} \rightarrow \text{Mn}^{3+}$ reduction process increases the B–O length and, therefore,

Received: November 7, 2012

Revised: January 21, 2013



changes the tolerance factor. Actually, the $\text{BaMnO}_{3-\delta}$ ^{7–11} and $\text{SrMnO}_{3-\delta}$ ⁶ systems exhibit a wide variety of structure types and extensive ranges of stoichiometry. In this sense, following the investigations of Negas and Roth,^{5–7} Jacobson and Horrox¹² studied the oxygen vacancy distribution in 4H- $\text{Ba}_{0.5}\text{Sr}_{0.5}\text{MnO}_{2.84}$, and later on, Adkin and Hayward expanded the range of oxygen deficiency down to 4H- $\text{Ba}_{0.5}\text{Sr}_{0.5}\text{MnO}_{2.79}$ ¹³ and, via the topotactic reduction of 4H- $\text{Ba}_{0.5}\text{Sr}_{0.5}\text{MnO}_{3-\delta}$ with LiH, stabilized Mn(II) in tetrahedral sites in 4H- $\text{Ba}_{0.5}\text{Sr}_{0.5}\text{MnO}_{2+\delta}$.¹⁴

Following these ideas we have investigated polytypism in a wide range of systems.^{15–18} Thus, by introducing compositional variations at the B sublattice in order to modify the *t* value, several polytypes have been stabilized in the oxygen-deficient $\text{BaMn}_{1-x}\text{Fe}_x\text{O}_{3-\delta}$ system. In the Mn rich area, V. Caignaert et al.¹⁹ reported the existence of a 6H' (hchhhc) polytype in the ($0 < \delta < 0.3$) compositional range. Later on, the crystal and magnetic structures and electrical properties of two new 6H' polytypes ($\text{BaMn}_{0.85}\text{Fe}_{0.15}\text{O}_{2.87}$ and $\text{BaMn}_{0.6}\text{Fe}_{0.4}\text{O}_{2.72}$)²⁰ were reported. On the other hand, a detailed structural characterization of a Fe-rich composition, 10H- $\text{BaMn}_{0.4}\text{Fe}_{0.6}\text{O}_{2.73}$,^{21,22} showed that although the basic structure is similar to that of 10H- $\text{BaFeO}_{3-\delta}$,²³ differences involving both the crystal structure and anionic vacancy distribution are present in the mixed Mn/Fe phase. These differences can involve short-range ordering phenomena which are crucial for understanding the behavior of the material. Up to now, microstructural characterization has been performed by means of high resolution electron microscopy (HREM) which provides coherent contrast which does not allow direct interpretation of images in terms of atomic potential. Image processing and calculation are required in order to achieve a correct image interpretation. Energy-dispersive X-ray spectroscopy (EDS) and electron energy loss spectroscopy (EELS) techniques provide very useful and complementary information in terms of local composition but not at the atomic level. Nevertheless, using scanning transmission electron microscopy (STEM) and a high angle annular dark field (HAADF) detector makes it possible to obtain so-called Z contrast images where the intensity in each point is roughly dependent only on the atomic number ($\sim Z^{3/2}$) and on the thickness of the specimen. For atomically resolved STEM, if we assume that the thickness is reasonably small and constant locally then the intensity in the Z contrast image of a specific atomic column will depend only on the atomic number and the occupancy in that column. The availability of Cs corrected microscopes pushed dramatically the limits of spatial resolution²⁴ making sub-angstrom imaging a routine exercise. Combining probe Cs corrector with a high brightness field emitter allowed researchers to obtain atomically resolved chemical mapping.^{25–27} Due to the ability to form a small probe with enough current even at very low acceleration voltage, the new tools enabled atomically resolved chemical mapping for very sensitive specimen such as carbon based material or single atomic sheet materials pushing the analytical limits at the level of a single atom.²⁸ According to these ideas, this is a powerful technique to study local phenomena associated with the compositional modification in hexagonal perovskites. Although this tool has been shown to be very efficient to distinguish local compositional variations in a corrected microscope, it has been mainly focused, until now, on solving problems in artificial grown heterostructures.

Attempts to stabilize the 4H-type by modifying the Mn:Fe ratio or by introducing different concentration of anionic

vacancies were unsuccessful. Nevertheless, in this paper we report a new Fe-rich 4H polytype within the $\text{BaMn}_{1-x}\text{Fe}_x\text{O}_{3-\delta}$ system obtained by doping at the A sublattice. This adds new compositional and microstructural complexities which will be precisely characterized by conventional and advanced tools as described above.

EXPERIMENTAL SECTION

$\text{Ba}_{0.8}\text{Sr}_{0.2}\text{Mn}_{0.4}\text{Fe}_{0.6}\text{O}_{3-\delta}$ was prepared by conventional solid state reaction from BaCO_3 (Sigma-Aldrich, 99.98%), SrCO_3 (Sigma-Aldrich, 99.9%), MnCO_3 (Sigma-Aldrich, 99%), and Fe_2O_3 (Sigma-Aldrich, 99.98%). A well-ground stoichiometric mixture of these reactants was decarbonated in air in a muffle furnace at 1173 K for 72 h, reground, and then heated in a Pt crucible at 1473 K in air for 2 days. The same process was repeated at 1573 K. Finally, the powder was heated at 1628 K for 60 h with intermediate grindings and then quenched to room temperature in air.

The average cation composition of the powder was determined by inductive coupling plasma (ICP) whereas the local composition was analyzed by EDS with an INCA analyzer system attached to a JEOL 3000 FEG electron microscope.

Powder X-ray diffraction (XRD) patterns were collected using Cu $K\alpha$ monochromatic radiation ($\lambda = 1.540\text{56 }\text{\AA}$) at room temperature on a Panalytical X'PERT PRO MPD diffractometer equipped with a germanium 111 primary beam monochromator and X'Celerator fast detector, while measurements with temperature were performed on a Panalytical X'PERT PRO MPD diffractometer equipped with an Anton Paar HTK1200 high temperature camera. Neutron diffraction (ND) data were collected at room temperature (RT) on the high resolution powder diffractometer D2B at the Institute Laue Langevin (ILL, Grenoble, France) with neutrons of wavelength 1.594 \AA . The angular range covered by the detectors extends from 0° to 160° with a step size of 0.05° . Neutron diffraction data were collected from sample at different temperatures on the high flux D1B instrument. Diffraction data were analyzed by the Rietveld method²⁹ using the Fullprof program.³⁰

Selected area electron diffraction (SAED) and HREM were performed using a JEOL 3000 FEG electron microscope, fitted with a double tilting goniometer stage ($\pm 22^\circ$, $\pm 22^\circ$). Simulated HREM images were calculated by the multislice method using the MacTempas software package. Atomically resolved HAADF images and EELS maps were obtained in a Titan³ G2 60-300 TEM microscope equipped with Cs aberration corrector for the probe forming optics as well for the imaging system. The microscope was fitted with a monochromator and a Quantum 966 GIF. The experiments were performed at 300 kV using a semiconvergence angle of about 21 mrads and a collection angle for the EELS signal of about 120 mrads.

Direct current magnetization was measured in a SQUID magnetometer, in the range ~ 2 –300 K under an applied magnetic field of 1000 Oe. The field dependence of the magnetization at 2 K was carried out in the range 0–50 kOe.

RESULTS AND DISCUSSION

Structural Study. The cationic composition of the sample, determined on several dozens of small crystallites by EDS analysis in the electron microscope, is in agreement with the nominal one (see Supporting Information, Figure I). The oxygen content was obtained from the analysis of the neutron diffraction data and will be discussed below.

The XRD pattern of $\text{Ba}_{0.8}\text{Sr}_{0.2}\text{Mn}_{0.4}\text{Fe}_{0.6}\text{O}_{3-\delta}$ can be indexed on the basis of a hexagonal unit cell with $P6_3/mmc$ space group and cell parameters $a = 5.6998(1)$, $c = 9.5115(2)\text{ \AA}$ (Figure II, SI). The lattice parameters are consistent with a hexagonal 4H-polytype.⁵ Stacking faults are a common occurrence in these polytypic materials and are easily detected by SAED and HREM. Figure 1 a,b shows the electron diffraction patterns along [1–10] and [010], respectively, indexed on the basis of

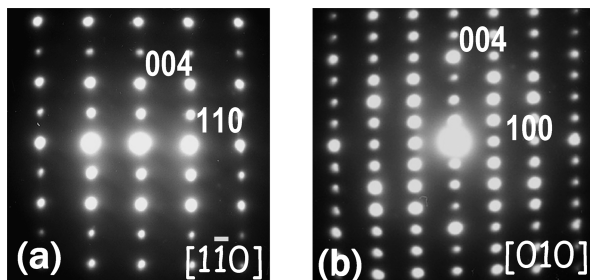


Figure 1. SAED pattern along zone axes (a) $[1\bar{1}0]$ and (b) $[010]$ corresponding to $\text{Ba}_{0.8}\text{Sr}_{0.2}\text{Mn}_{0.4}\text{Fe}_{0.6}\text{O}_{2.70}$.

the previous cell. The presence of extended defects can be discarded since all diffraction spots appear sharp and without any apparent streaking along the c^* axis. The layer sequence of the polytype can be directly obtained from the corresponding $[010]$ HREM image (Figure 2). The image simulation, inset of

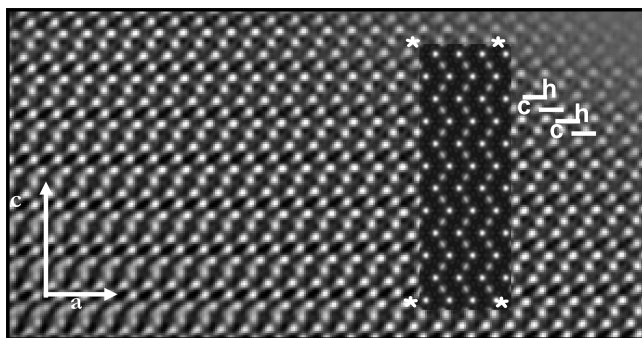


Figure 2. $[010]$ HREM image corresponding to $\text{Ba}_{0.8}\text{Sr}_{0.2}\text{Mn}_{0.4}\text{Fe}_{0.6}\text{O}_{2.70}$. The simulated image can be observed at the inset.

Figure 2, fits perfectly with the experimental one for $\Delta f = -5$ nm and $\Delta t = 5$ nm. In this zone, the structure is viewed parallel to the columns of Ba–O close packed rows, and the stacking sequence of the layers is revealed directly. According to this, the observed contrast of the image can be interpreted as corresponding to a (...hchc...) layer arrangement. The sequence is extended over the whole crystal confirming that the stabilized phase is homogeneous and apparently ordered. In order to get more detailed information at atomic level, a STEM and EELS study was performed in a Cs corrected microscope.

In the atomically resolved HAADF image (Figure 3), the heaviest elements (Ba and Sr) can be identified as the brightest atomic columns while the Fe and Mn columns of atoms are observed as less bright spot and the positions of the columns fit with the proposed model. Due to the high spatial resolution one can notice that both A and B positions are perfectly resolved and atomic columns separated by 0.17 nm and different atomic numbers are clearly identified.

In order to identify unambiguously the atomic species, an EELS spectrum imaging data set was acquired (see Figure 4). The spectrum imaging was acquired in STEM by rastering the beam over the area of interest marked in Figure 4a ($\sim 60 \text{ nm}^2$) to simultaneously record the HAADF image displayed in Figure 4b and single EELS spectrum from each point. A summed spectrum from 800 points (see Figure 4c) shows the characteristic edges used to generate the chemical maps of the elements of interest (Ba–Mn–Fe–O) with the exception of the Sr-signal. The poor signal-to-background nature of the

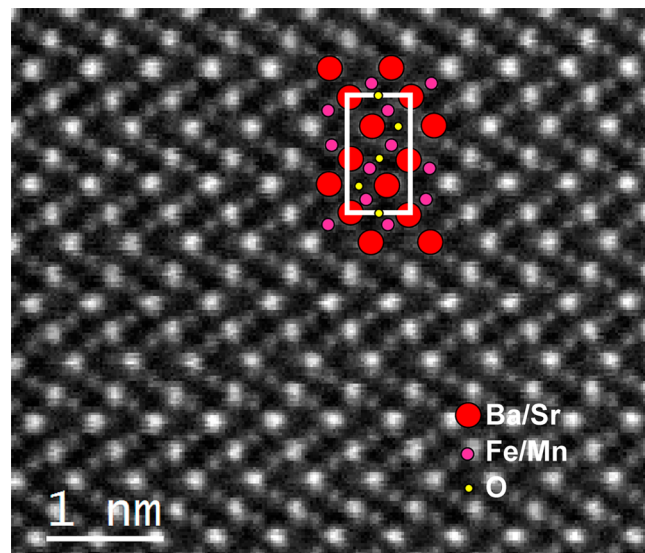


Figure 3. Atomically resolved HAADF image along $[010]$ zone axis. Schematic atomic model is included.

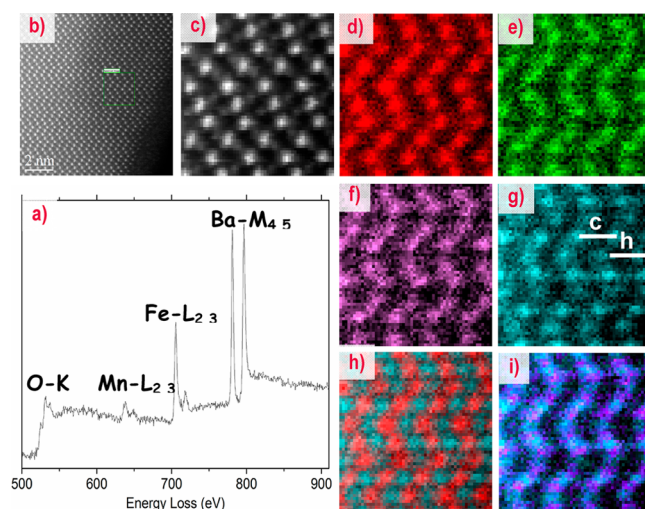


Figure 4. Atomic resolution EELS maps. (a) Z contrast survey image of the specimen. (b) Z contrast image of the region of interest from where the EELS signal was acquired (marked with a green square in image a). (c) Spectrum obtained from summing the EELS signal a few pixels from the region of interest. (d) Ba chemical map. (e) Mn chemical map. (f) Fe chemical map. (g) O chemical map, hexagonal and cubic layers are marked. (h) Ba and O composite map. (i) Fe and O composite map.

Sr-M_{2,3} edge (at 133 eV) and the high value of energy loss for the Sr-L_{2,3} edge (1994 eV) prevented the simultaneous acquisition of these signals. The atomic-resolution elemental maps of the sample are shown in Figure 4d–i. For each point of the spectrum image, the characteristic signal for each edge was integrated after background subtraction, and the intensity of the four distinct elements is translated into a color code: Ba (red), Mn (green), and Fe (pink), and O (light blue). This allows us to identify the distribution of the above-mentioned elements in the sample. Notice that the A, B, and O atomic columns are nicely resolved (Figure 4d,g,i). From the chemical maps a random distribution of Mn and Fe cations is observed in the B-sites while Ba signal is detected for the A-sites. Moreover, a difference in contrast can be observed in the oxygen mapping

Table 1. Structural Parameters from the Refinement for 4H-Ba_{0.8}Sr_{0.2}Mn_{0.4}Fe_{0.6}O_{2.70}

	<i>x</i>	<i>y</i>	<i>z</i>	<i>B</i> _{iso} (Å ²)	occ
Ba/Sr(1)	0	0	0	<i>c</i>	0.80(1)/0.20(1) ^a
Ba(2)	1/3	2/3	0.25	0.99(7)	1
M	1/3	2/3	0.5902(2)	0.92(5)	0.39(1)/0.61(1) ^b
O(1)	0.5	0	0	1.10(3)	1
O(2)	-0.1823(5)	-0.3647(11)	0.25	1.90(5)	0.79(1)

^aBa/Sr. ^bFe/Mn. $R_B = 4.64$, $R_p = 2.65$, $R_{wp} = 3.55$, $R_{exp} = 1.83$, $\chi^2 = 3.78$. ^cAnisotropic temperature factor: $\beta_{11} = \beta_{22} = 0.0737(7)$, $\beta_{33} = 0.0229(7)$.

which is due either to the different coordination in hexagonal and cubic layers or to different oxygen concentration of those layers since this sample has oxygen deficiency. The contrast distribution suggests that less bright layers should be those with less oxygen content as expected for the hexagonal layers.^{19,31–33} Up to now, to identify random distribution of oxygen vacancies in a powdered ceramic was an unapproachable goal by conventional electron microscopy techniques. The combined use of HAADF and EELS in an aberration corrected microscope makes it possible to obtain this information layer by layer.

To get additional information on the features of the deficient hexagonal layers a neutron diffraction study was performed. The large contrast between the scattering lengths of Mn (-3.750 fm) and Fe (9.45 fm) and of Ba (0.5 fm) and Sr (0.7 fm) makes neutron diffraction a suitable tool for this purpose. The NPD data collected at room temperature were refined using the structural parameters of an ideal 4H polytype⁵ as a starting model. This structure is formed by two face sharing octahedral (M_2O_9) units which are sharing corners among them. The random occupancy of Fe and Mn elements as well as the presence of Ba in two A-type crystallographic positions was considered in the input structural model as it was deduced from the EELS data. The atomic coordinates, isotropic thermal parameters (except for Ba/Sr(1), see Table 1), and occupancy factors of all atoms were refined. The occupancy factors of the oxygen atoms reveal that the anionic sublattice is not complete; the full composition obtained was Ba_{0.80(1)}Sr_{0.20(1)}Mn_{0.40(1)}-Fe_{0.60(1)}O_{2.70(1)}. The Rietveld refinement pattern and difference plot for this sample is shown in Figure 5a. The obtained structural parameters are listed in Table 1, and selected interatomic distances are gathered in Table 2.

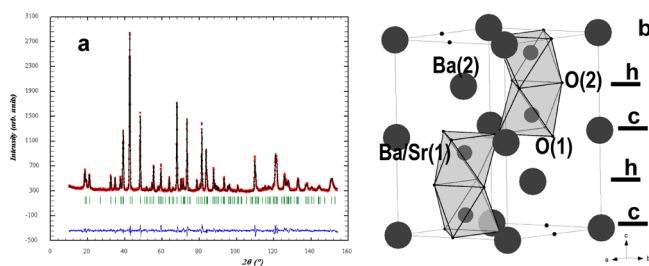


Figure 5. (a) Observed, calculated, and difference profile of neutron diffraction patterns for Ba_{0.8}Sr_{0.2}Mn_{0.4}Fe_{0.6}O_{2.70} at room temperature. (b) Structural model for 4H-Ba_{0.8}Sr_{0.2}Mn_{0.4}Fe_{0.6}O_{2.70}.

A schematic representation of the structure is depicted in Figure 5b. It is formed by dimers of face-sharing octahedra that are linked by corners. The obtained Mn:Fe ratio agrees with the nominal composition (see Table 1). The M–O distances (1.85 and 2.12 Å) are in excellent agreement with those observed in other dimers of octahedra in other polytypes of this system:

Table 2. Selected Interatomic Distances (Å) in 4H-Ba_{0.8}Sr_{0.2}Mn_{0.4}Fe_{0.6}O_{2.70}

Ba/Sr(1)–O	2.8516(2) × 6
Ba(2)–O	2.8918(3) × 6
M–O	1.8582(18) × 3
M–M	3.716(2)
M–M	3.032(5)

2.22 and 1.850 Å in 10H-BaMn_{0.4}Fe_{0.6}O_{2.73}²¹ or 2.175 and 1.783 Å in 6H'-BaMn_{0.85}Fe_{0.15}O_{2.87}²⁰. In all cases, the metal atoms (Mn, Fe) are displaced from the center of octahedron toward the adjacent cubic layer (Table 2) reducing the electrostatic repulsion between cations in adjacent face-sharing octahedra. This displacement is more pronounced than that observed in 4H-Ba_{1-y}Sr_yMnO_{3-δ}⁶ ($0 \leq y \leq 0.5$; $0 \leq \delta \leq 0.35$) where all octahedra are occupied by Mn. The presence of two cations, Mn and Fe, with slightly different size and different electronic configuration, Mn⁴⁺ (d³) and Fe³⁺ (d⁵), in the same crystallographic site can lead to an increase of the electrostatic repulsions and, therefore, to more distorted octahedra.

The Ba and Sr distribution along the different crystallographic positions is gathered in Table 1. The position 2, corresponding to the hexagonal layer, is fully occupied by Ba, whereas Sr and the remaining Ba are at position 1, corresponding to the cubic layer. The refinement of the isotropic temperature factor gives an anomalous value probably due to the presence of two cations with different size at the same crystallographic site. It was therefore necessary to refine the anisotropic temperature factors for this position. The Ba/Sr distribution can be explained on the basis of the different sizes of both cations ($r_{Ba^{2+}} = 1.61$ Å and $r_{Sr^{2+}} = 1.11$ Å);³⁴ for this reason, the smaller cation, Sr²⁺, is located at the cubic layers.

The refinement of the oxygen occupancy (Table 1) shows the presence of anionic vacancies randomly distributed in hexagonal layers as suggested by EELS atomic-resolution elemental maps (see Figure 4). The anionic composition for this layer is BaO_{2.4}. The preference of oxygen vacancies to be distributed along hexagonal layers has been previously observed in similar systems, as is the case of BaMnO_{3-δ}, BaMn_{1-x}Ti_xO_{3-δ}, and BaMn_{1-x}Fe_xO_{3-δ}. In general, the average distance $d(O–Ba)$ in the hexagonal layers is greater than in the cubic ones¹³ suggesting a lower bonding strength and, therefore, a higher possibility for the introduction of anionic vacancies in these layers. It is worth stressing that, in these polytypes, anionic vacancies are always distributed along the hexagonal layers. As we have shown, this is the situation in 4H-Ba_{0.8}Sr_{0.2}Mn_{0.4}Fe_{0.6}O_{2.70}. The same distribution appears in Ba_{0.5}Sr_{0.5}MnO_{2.79},³³ where the hexagonal layer shows the composition BaO_{2.56}. However, in BaMnO_{2.65},³⁵ isostructural

with the two previous, anionic vacancies are present in both layers, hexagonal and cubic, whose compositions are $\text{BaO}_{2.28}$ and $\text{BaO}_{2.91}$, respectively. This suggests that the hexagonal layer supports a maximum number of vacancies, around $\delta = 0.7$; therefore, for higher δ values, vacancies are accommodated along the cubic layers. This could be explained taking into account the shield effect of the oxygen in the hexagonal layers since it seems to be necessary to have a minimum oxygen amount to reduce repulsion between metals in order to ensure the stability of the structure.

The oxygen content suggests that the average oxidation state of metals at the B sites corresponds to $M^{3.4+}$, which indicates the presence of 40% of metals in IV oxidation state and 60% in III. In the most oxidized phases of this system, $6\text{H}'\text{-BaMn}_{1-x}\text{Fe}_x\text{O}_{3-\delta}$ ²⁰ and $10\text{H}\text{-BaMn}_{0.4}\text{Fe}_{0.6}\text{O}_{2.73}$,²¹ Mn is in IV, and the decreasing of the oxygen content is only accompanied by the partial reduction from Fe^{4+} to Fe^{3+} . This seems to indicate that, in the reduction process, Fe is reduced before Mn, thus allowing us to propose the following composition for the new 4H phase: $\text{Ba}_{0.8}\text{Sr}_{0.2}\text{Mn}^{\text{IV}}_{0.4}\text{Fe}^{\text{III}}_{0.6}\text{O}_{2.70}$.

Magnetic Behavior. Magnetic susceptibility measurements performed as a function of the temperature (Figure 6) show a

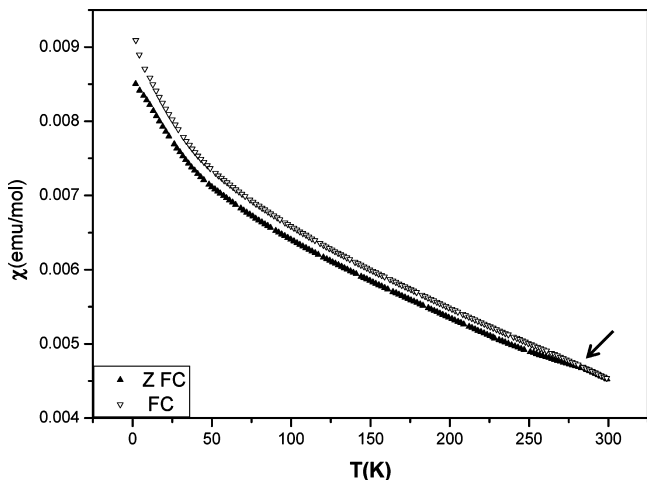


Figure 6. ZFC and FC magnetic susceptibility data for $\text{Ba}_{0.8}\text{Sr}_{0.2}\text{Mn}_{0.4}\text{Fe}_{0.6}\text{O}_{2.70}$.

divergence between zero-field-cooled (ZFC) and field-cooled (FC) data, below 290 K for $\text{Ba}_{0.8}\text{Sr}_{0.2}\text{Mn}_{0.4}\text{Fe}_{0.6}\text{O}_{2.70}$, which may be associated with a magnetic transition of antiferromagnetic origin as previously observed in other Mn-based hexagonal perovskites, such as $\text{BaMnO}_{3-\delta}$ ³⁶ 4H-SrMnO₃,³⁷ and 4H-(Ba,Sr)MnO_{3-δ}.³³

The variation of magnetization with a magnetic field at 5 K is shown in Figure 7 where a hysteresis loop can be observed (discussed below). To get additional information about the magnetic features of these phases, variable temperature neutron diffraction data were collected on the high flux instrument D1B.

Extra intensity not accounted for by the structural model was evident in (002), (101), (102), and (112) reflections at temperatures below 270 K. These contributions to the diffraction pattern were analyzed by considering they were magnetic in origin and could be accounted for by the $P6_3/mmc$ space group with a magnetic unit cell of the same dimensions as the structural one (propagation vector, $k = 0$).

The atomic coordinates were fixed, and only the lattice parameters, profile parameters, and magnetic moments were

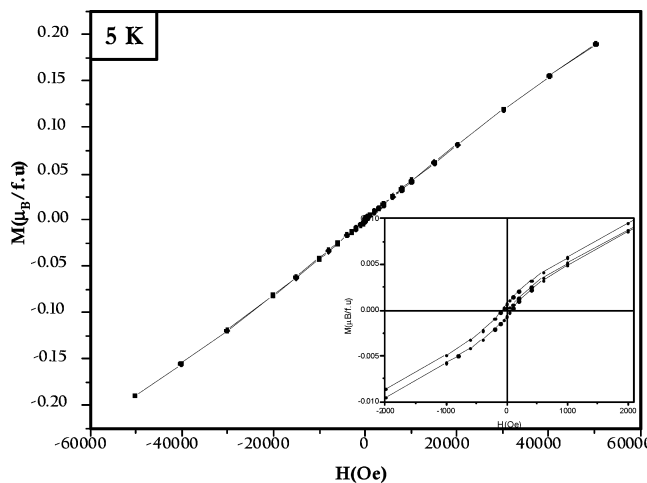


Figure 7. Magnetization versus magnetic field at 5 K for $\text{Ba}_{0.8}\text{Sr}_{0.2}\text{Mn}_{0.4}\text{Fe}_{0.6}\text{O}_{2.70}$.

refined. Both cations, Mn and Fe, were considered to take part in the long-range magnetic ordering as previously observed in $6\text{H}'\text{-BaMn}_{1-x}\text{Fe}_x\text{O}_{3-\delta}$.²⁰ Several models were tested; the best fit was obtained from a magnetic model which assumes antiferromagnetic interactions between nearest neighbors (NN). Figure 8 shows the fitting at 150 K. The model results

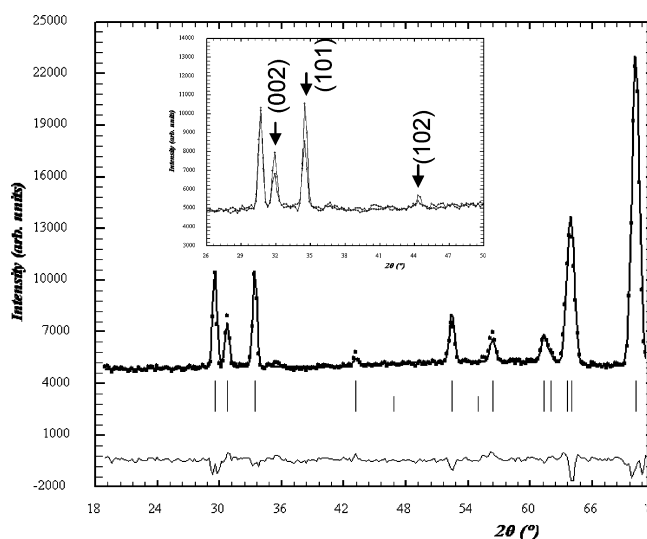


Figure 8. Fitting of the neutron diffraction data for $\text{Ba}_{0.8}\text{Sr}_{0.2}\text{Mn}_{0.4}\text{Fe}_{0.6}\text{O}_{2.70}$ ($R_B = 4.57$, $R_{\text{mag}} = 6.37$, $\chi^2 = 3.07$) at 150 K.

in a magnetic structure consisting of ferromagnetic sheets with the magnetic moments aligned along the x -axis and coupled antiferromagnetically along the c -axis (Figure 9). The thermal variation of the magnetic moments per unit formula obtained from the refinement is shown in Figure 10. According to these data the magnetic moment increases at $T < 270$ K and keeps constant at $T \sim 220$ K, with a $T_N \sim 270$ K being obtained, similar to those observed in the 4H-Ba_{1-x}Sr_xMnO_{3-δ} phases,¹² with T_N values between 200 and 280 K. These results are consistent with the observed divergence between FC and ZFC data of the magnetic susceptibility (Figure 6).

The value of the refined magnetic moment 5 K, ca. $1.3 \mu_B$ per unit formula, is lower than the predicted value for Mn^{IV} allowing for a degree of covalency,³⁸ ca. $2.6 \mu_B$, and lower

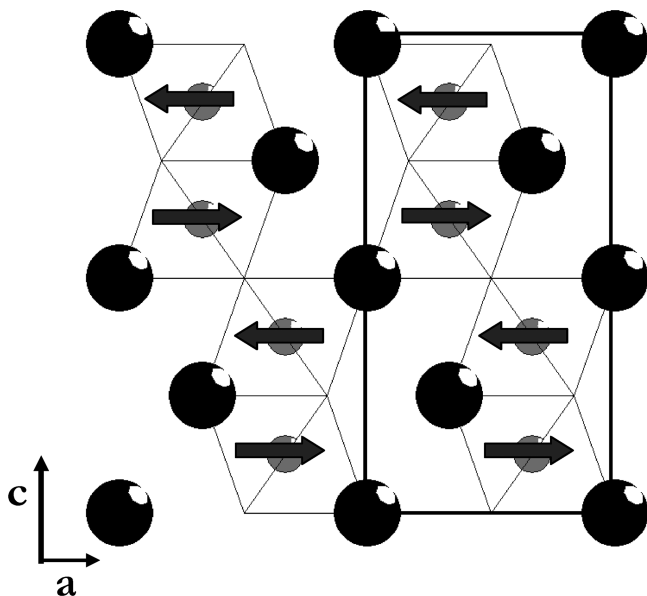


Figure 9. Antiferromagnetic structure of $\text{Ba}_{0.8}\text{Sr}_{0.2}\text{Mn}_{0.4}\text{Fe}_{0.6}\text{O}_{2.70}$.

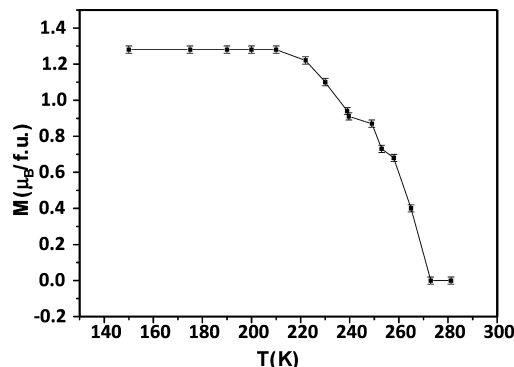


Figure 10. Thermal variation of the magnetic moments per formula unit obtained from the refinement corresponding to $\text{Ba}_{0.8}\text{Sr}_{0.2}\text{Mn}_{0.4}\text{Fe}_{0.6}\text{O}_{2.70}$.

than the expected for Fe^{III} , $\mu_{\text{calc}} = 5.099 \mu_{\text{B}}$ per unit formula. This feature is also observed in all the above-mentioned Mn-phases, and it has been ascribed to partial magnetic frustration, originating from competing interactions in some metallic sites occupied by both Fe and Mn ions. Actually, the random distribution of Mn and Fe over the octahedral sites allows the following 90° or 180° superexchange interactions via bridging oxygen, e.g., $\text{Mn}^{\text{IV}}(\text{d}^3)-\text{O}-\text{Mn}^{\text{IV}}(\text{d}^3)$, $\text{Fe}^{\text{III}}(\text{d}^5)-\text{O}-\text{Fe}^{\text{III}}(\text{d}^5)$, $\text{Mn}^{\text{IV}}(\text{d}^3)-\text{O}-\text{Fe}^{\text{III}}(\text{d}^5)$ along the chain. Considering that the first two are antiferromagnetic but the latter is ferromagnetic,³⁹ competing interactions could be present leading to magnetic frustration which may be responsible for the hysteresis loop observed at 5 K (Figure 7).

It is worth noting this magnetic model is rather common in Mn-containing hexagonal polytypes with mixed hexagonal and cubic layers. Isostructural 6H'- $\text{BaMnO}_{3-\delta}$ ⁴ and 6H'- $\text{BaMn}_{1-x}\text{Fe}_x\text{O}_{3-\delta}$ adopt the same magnetic structure indicating the partial Mn substitution for Fe does not modify significantly the magnetic cation arrangement. Moreover, a similar magnetic model is obtained in other Mn-based hexagonal polytypes regardless of the particular stacking sequence(s). For instance, 4H- BaMnO_3 ²⁴ and 15R- $\text{SrMn}_{0.9}\text{Fe}_{0.1}\text{O}_{3-\delta}$ ⁴⁰ have a similar arrangement scheme with antiferromagnetic interactions in

the face-sharing octahedral blocks giving rise to ferromagnetic sheets perpendicular to the c -axis. However, this 3D order is not found in 2H- BaMnO_3 ³⁶ (only hexagonal layers), despite the antiferromagnetic coupling between Mn^{IV} ions in the rows of face-sharing octahedra. This result should be indicative that the general features of the magnetic model proposed for this 4H polytype may be general behavior for all of the hexagonal polytypes with NN antiferromagnetic interactions between transition metal cations.

CONCLUSION

Obtaining atomic structural and chemical information is proven to be an invaluable tool to directly observe cation and anionic distribution in powdered materials. The use of an aberration corrected microscope has allowed us to obtain unveiling structural and compositional details with an unprecedented precession in bulk hexagonal perovskite related materials. Enhanced single atom sensitivity in terms of imaging and spectroscopy has been exploited for the structural characterization of a new Fe-rich 4H phase within the $\text{BaMn}_{1-x}\text{Fe}_x\text{O}_{3-\delta}$ system, $\text{Ba}_{0.8}\text{Sr}_{0.2}\text{Mn}^{\text{IV}}_{0.4}\text{Fe}^{\text{III}}_{0.6}\text{O}_{2.70}$. The structure is formed by dimers of face-sharing octahedra that are linked by corners. In this sense, the different A (Ba) and B (Mn and Fe) cationic positions are clearly resolved in the HAADF images, being unambiguously identified by means of EELS spectral imaging. This study shows a random distribution of the Fe and Mn cations and provides information about the oxygen arrangement since two kinds of contrast appear in the corresponding mapping. ND data provides the quantification of the oxygen content in the layers confirming that the oxygen deficiency is distributed along the hexagonal layers as suggested by EELS spectral imaging. Neutron diffraction data suggest a complex magnetic structure formed by ferromagnetic sheets with the magnetic moments aligned along the x -axis and stacked antiferromagnetically perpendicular to the c -axis.

ASSOCIATED CONTENT

Supporting Information

Additional figures. This material is available free of charge via the Internet at <http://pubs.acs.org>.

AUTHOR INFORMATION

Corresponding Author

*E-mail: jgcalbet@quim.ucm.es (J.M.G.-C.), mparras@quim.ucm.es (M.P.). Fax: (34) 91 394 43 52.

Author Contributions

The authors contributed equally.

Notes

The authors declare no competing financial interest.

ACKNOWLEDGMENTS

Financial support from Ministerio de Economía (Spain) through research projects MAT2007-61954, CSD2009-00013, and MAT2011-23068 is acknowledged. Electron microscopy has been performed in the National Centre for Electron Microscopy (Campus de Excelencia Moncloa-UCM). Corrected aberration images have been obtained in a Titan G2 60-300 TEM FEI electron microscope. The authors gratefully acknowledge Dr. A. Alarcón and FEI Company for facilities. We thank Dr. M. T. Fernández-Díaz for assistance in collecting neutron powder diffraction data.

ABBREVIATIONS

c, cubic; h, hexagonal; HREM, high resolution electron microscopy; EDS, energy-dispersive X-ray spectroscopy; EELS, electron energy loss spectroscopy; STEM, scanning transmission electron microscopy; HAADF, high angle annular dark field; ICP, inductive coupling plasma; XRD, powder X-ray diffraction; ND, neutron diffraction; SAED, selected area electron diffraction; ZFC, zero-field-cooled; FC, field-cooled; NN, nearest neighbors

REFERENCES

- (1) Feteira, A.; Sarma, K.; Alford, N. McN.; Reaney, I. M.; Sinclair, D. *C. J. Am. Ceram. Soc.* **2003**, *86*, 511–513.
- (2) Keith, G. M.; Kirk, C. A.; Sarma, K.; Alford, N.; Cussen, E. J.; Rosseinsky, M. J.; Sinclair, D. C. *Chem. Mater.* **2004**, *16*, 2007–2015.
- (3) Goldschmidt, V. M. *Naturwissenschaften* **1926**, *14*, 477–485.
- (4) Hardy, A. *Acta Crystallogr.* **1962**, *15*, 175–179.
- (5) Negas, T.; Roth, R. S. *J. Solid State Chem.* **1970**, *1*, 409–418.
- (6) Negas, T. *J. Solid State Chem.* **1973**, *6*, 136–150.
- (7) Negas, T.; Roth, R. S. *J. Solid State Chem.* **1971**, *3*, 323–339.
- (8) González-Calbet, J. M.; Parras, M.; Alonso, J. M.; Vallet-Regí, M. *J. Solid State Chem.* **1993**, *106*, 99–110.
- (9) González-Calbet, J. M.; Parras, M.; Alonso, J. M.; Vallet-Regí, M. *J. Solid State Chem.* **1994**, *111*, 202–207.
- (10) Parras, M.; González-Calbet, J. M.; Alonso, J. M.; Vallet-Regí, M. *J. Solid State Chem.* **1994**, *113*, 78–87.
- (11) Parras, M.; Alonso, J. M.; González-Calbet, J. M.; Vallet-Regí, M. *J. Solid State Chem.* **1995**, *117*, 21–29.
- (12) Jacobson, A. J.; Horrox, J. W. *Acta Crystallogr., Sect. B* **1976**, *32*, 1003–1008.
- (13) Adkin, J. J.; Hayward, M. A. *Chem. Mater.* **2007**, *19*, 755–762.
- (14) Adkin, J. J.; Hayward, M. A. *Inorg. Chem.* **2008**, *47*, 10959–10964.
- (15) Miranda, L.; Feteira, A.; Sinclair, D. C.; García Hernández, M.; Boulahya, K.; Hernando, M.; Varela, A.; González-Calbet, J. M.; Parras, M. *Chem. Mater.* **2008**, *20* (8), 2818–2828.
- (16) Miranda, L.; Feteira, A.; Sinclair, D. C.; Boulahya, K.; Ramírez, J.; Hernando, M.; Varela, A.; González-Calbet, J. M.; Parras, M. *Chem. Mater.* **2009**, *21* (8), 1731–1742.
- (17) Miranda, L.; Sinclair, D. C.; Hernando, M.; Varela, A.; Ramírez, J.; Boulahya, K.; González-Calbet, J. M.; Parras, M. *Chem. Mater.* **2010**, *22*, 4320–4327.
- (18) Miranda, L.; Boulahya, K.; Hernando, M.; Sinclair, D. C.; Jiménez-Villacorta, F.; Varela, A.; González-Calbet, J. M.; Parras, M. *Chem. Mater.* **2011**, *23* (4), 1050–1060.
- (19) Caignaert, V.; Hervieu, M.; Domengès, B.; Nguyen, N.; Pannetier, J.; Raveau, B. *J. Solid State Chem.* **1988**, *73*, 107–117.
- (20) Miranda, L.; Sinclair, D. C.; Hernando, M.; Varela, A.; Wattiaux, A.; Boulahya, K.; González-Calbet, J. M.; Parras, M. *Chem. Mater.* **2009**, *21* (21), 5272–5283.
- (21) Miranda, L.; Boulahya, K.; Varela, A.; González-Calbet, J. M.; Parras, M.; Hernando, M.; Fernández, M. T.; Feteira, A.; Sinclair, D. C. *Chem. Mater.* **2007**, *19* (14), 3425–3432.
- (22) Miranda, L.; Ramírez, J.; Hernando, M.; Varela, A.; González-Calbet, J. M.; Parras, M. *Eur. J. Inorg. Chem.* **2007**, *15*, 2129–2135.
- (23) Delattre, J.; Stacy, A. M.; Siegrist, T. *J. Solid State Chem.* **2004**, *177*, 928–935.
- (24) Kisielowski, C.; Freitag, B.; Bischoff, M.; van Lin, H.; Lazar, S.; Knippels, G.; Tiemeijer, P.; van der Stam, M.; von Harrach, S.; Stekelenburg, M.; Haider, M.; Muller, H.; Hartel, P.; Kabius, B.; Miller, D.; Petrov, I.; Olson, E.; Donchev, T.; Kenik, E. A.; Lupini, A.; Bentley, J.; Pennycook, S.; Minor, A. M.; Schmid, A. K.; Duden, T.; Radmilovic, V.; Ramasse, Q.; Erni, R.; Watanabe, M.; Stach, E.; Denes, P.; Dahmen, U. *Microsc. Microanal.* **2008**, *14*, 454–462.
- (25) Kimoto, K.; Asaka, T.; Nagai, T.; Saito, M.; Matsui, Y.; Ishizuka, K. *Nature* **2007**, *450*, 702–704.
- (26) Muller, D. A. *Nat. Mater.* **2009**, *8*, 263–270.
- (27) Botton, G.; Lazar, S.; Dwyer, C. *Ultramicroscopy* **2010**, *110*, 926–934.
- (28) Krivanek, O. L.; Dellby, N.; Murfitt, M. F.; Chisholm, M. F.; Pennycook, T. J.; Suenaga, K.; Nicolosi, V. *Ultramicroscopy* **2010**, *110*, 935–945.
- (29) Rietveld, H. M. *J. Appl. Crystallogr.* **1969**, *2*, 65–71.
- (30) Rodríguez- Carvajal, J. *J. Phys. B* **1993**, *192*, 55–69.
- (31) Jacobson, A. J. *Acta Crystallogr., Sect. B* **1976**, *32*, 1087–1090.
- (32) Sinclair, D. C.; Skakle, J. M. S.; Morrison, F. D.; Smith, R. I.; Beales, T. P. *J. Mater. Chem.* **1999**, *9*, 1327–1331.
- (33) Adkin, J. J.; Hayward, M. A. *Chem. Mater.* **2007**, *19*, 755–762.
- (34) Shannon, R. D. *Acta Crystallogr.* **1976**, *A32*, 751–767.
- (35) Hadermann, J.; Abakumov, A. M.; Adkin, J. J.; Hayward, M. A. *J. Am. Chem. Soc.* **2009**, *131* (30), 10598–604.
- (36) Cussen, E. J.; Battle, P. D. *Chem. Mater.* **2000**, *12*, 831–838.
- (37) Battle, P. D.; Gibb, T. C.; Jones, C. W. *J. Solid State Chem.* **1988**, *74*, 60–66.
- (38) Tofield, B. C.; Fender, B. E. F. *J. Phys. Chem. Solids* **1971**, *31*, 2741–2749.
- (39) *Magnetism and the Chemical Bond*; Goodenough, J. B., Ed.; John Wiley and Sons: New York, 1963.
- (40) Cussen, E. J.; Sloan, J.; Vente, J. F.; Battle, P. D.; Gibb, T. C. *Inorg. Chem.* **1998**, *37* (23), 6071–6077.